Supplementary Materials for

Tunable Nonthermal Distribution of Hot Electrons in a Semiconductor Injected from a Plasmonic Gold Nanostructure

Scott Kevin Cushing,[†, ‡] Chih-Jung Chen,[§] Chung Li Dong,[∥] Xiang-Tian Kong,[⊥,∇] Alexander O. Govorov,[∇] Ru-Shi Liu, [§, o,*] and Nianqiang Wu[†,*]

[†] Department of Mechanical and Aerospace Engineering and [‡] Department of Physics and Astronomy, West Virginia University, Morgantown, WV 26506, United States

[§] Department of Chemistry, National Taiwan University, Taipei 10617, Taiwan

[∥] Department of Physics, Tamkang University, Tamsui 25137, Taiwan

[⊥] Institute of Fundamental and Frontier Sciences and State Key Laboratory of Electronic Thin Films and Integrated Devices, University of Electronic Science and Technology of China, Chengdu 610054, China

[∇] Department of Physics and Astronomy, Ohio University, Athens, Ohio 45701, United States

[o] Department of Mechanical Engineering and Graduate Institute of Manufacturing Technology, National Taipei University of Technology, Taipei 10617, Taiwan

*Corresponding authors: Email: nick.wu@mail.wvu.edu; rsliu@ntu.edu.tw.

This PDF file includes:

Figs. S1 to S5
References S1-14

Materials and Methods

Section 1: Materials and characterization

The core-shell Au@TiO_2 nanoparticles were synthesized as shown in our previous paper.[1] The particle morphology was observed using a transmission electron microscope (TEM, JEOL, JEM 2100) and can be seen in Figure S1. In general, the samples consisted of a metallic core (sphere, rod, star) with 10-30 nm characteristic size and a 10 nm TiO_2 shell. The light absorption spectra were taken with a Shimazdu 2550 spectrometer in aqueous solution.

Section 2: X-ray absorption measurements and processing

All the X-ray absorption measurements were conducted at the National Synchrotron Radiation Research Center (NSRRC) in Hsinchu, Taiwan. The Ti L-edge spectra were characterized at the BL20A1 beamline. The spectra were taken with total electron yield mode. The geometry of XAS experiment is illustrated by the following figure. The distance between the sample holder and the chamber window is approximately 20 cm. The length from the Xe lamp (500 W) to the sample holder is about 1 m. The power density of incident light on samples was ~200 mW/cm^2 estimated by setting a power meter 1 m away from the lamp. However, samples were not directly illuminated by the incident light because they were tilted for the XAS measurement, the lamp was spectrally filtered, and non-AR coated optics were used as the entrance windows. This leaves an excitation power density covering the plasmonic peak on the order of ~10 mW/cm^2. The acquisition time of XAS experiment was 48 s per spectrum. The collected XAS spectrum was first subtracted by a straight line which is below the rising absorption edge to exclude the background generated by the incoming x-rays. Then, to compare the spectra with each other, all the spectra were normalized at the continuum states (about energy above 470 eV) where no fine absorption features are expected.

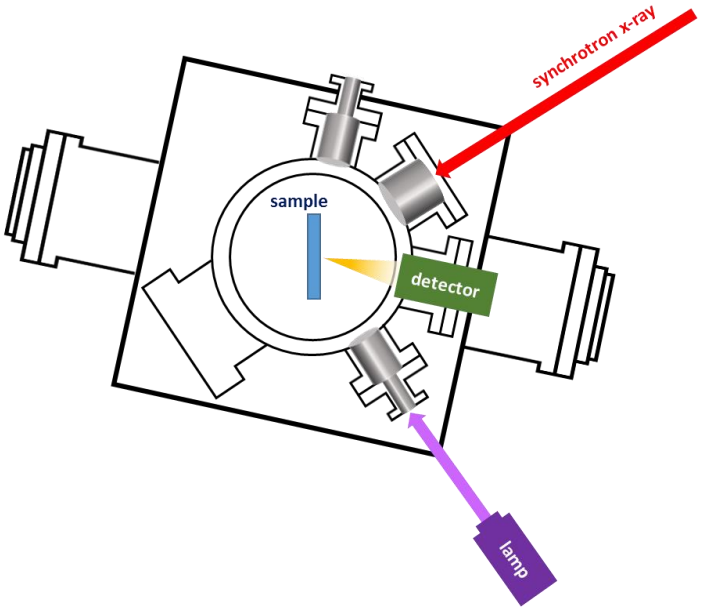

Schematic of the geometry of XAS experiment.

Section 3: Theoretical Prediction of Ground State X-ray Absorption

The ground and excited state X-ray absorption was calculated within the OCEAN code (Obtaining Core-level Excitations using Ab initio methods and the NIST BSE solver.[2,3] The density functional level was used to calculate the ground state electron densities and wave-functions using Quantum-ESPRESSO.[4] In the OCEAN code, projector augmented wave (PAW) reconstructed wave functions are used to estimate the core-level transition matrix elements. The dielectric screening is estimated using a real-space random phase approximation inside a sphere around the atom along with a Levine-Louie model dielectric function outside the sphere.[5,6] The final electron-hole states are then calculated by the Bethe-Salpeter (BSE) equation.

The DFT density of states was calculated within the local density approximation (LDA) using a norm-conserving Perdew-Wang pseudopotential, a converged k-point mesh within the experimental broadening of 6x6x4 points, and a plane wave cutoff of 100 Ry. The TiO_2 was treated as anatase, with a relaxed *a* lattice constant of 3.75 Angstroms and *c* lattice constant of 9.38 Angstroms. For the BSE-DFT calculations, the final and projector augmented wave states were converged to the experimental absorption at k-point meshes of 6x6x4 and 2x2x2, respectively. A dielectric constant of 31 was used, again approximating the TiO_2 as anatase. The number of bands for the final and projector augmented wave states were converged at 50 and 100, respectively. The BSE mesh was 6x6x6 with a cut-off radius of 4.0 Bohr. The SCF mixing was 0.8. The spin orbit splitting was found to best describe the experimental data at 5.65 eV. The approach to broadening is described in Section 6. Several different strains and expansions were tested, and while an isotropic expansion best described the data, a local strain or distortion cannot be ruled out.

To describe the excited state spectrum, the ground state absorption prediction was first modified for state-filling changes using the hot carrier distribution predicted in Section 4 and 5 as outlined in Section 6. These predictions gave the energy dependence of the hot carrier distribution transferred to the TiO_2. Next, the lattice heating changes and amplitude of the state-filling effects were predicted by best fitting a range of thermal expansions using the above parameters for the BSE-DFT calculations. The continuum background was removed using an arctangent function. For comparison of the thermal and nonthermal energetic carrier cases, an elevated temperature Fermi-Dirac distribution with the same peak energy and amplitude was considered as can be seen in Figure 3 of the main paper.

Section 4: Theoretical modeling of hot carrier distribution in metal nanoparticles

The electromagnetic modeling is done for gold nanocrystals embedded into a uniform medium with a dielectric constant of 2.2 to account for the TiO_2 shell. The empirical data from Reference (*7)* with the 5-times increased Drude broadening was used for the dielectric constant of gold[8]. The shapes and sizes of model nanocrystals (Figure S1) were taken from the experiment. The calculations were done using COMSOL and the resulting extinction spectra (Figure 2a in the main text) reproduce the experiment well.

The quantum theory of generation of hot carriers in nanocrystals predicts that the distribution of electrons in the steady-state of a plasmonic nanocrystal has certain

characteristic features.[9-11] These features are crucial for the understanding of the process of injection from a plasmonic nanoparticle to a neighboring object. Figure S4 shows a distribution of hot electrons in an optically-excited spherical nanoparticle made of gold. This calculation is done using the quantum theory and taken from Reference (*11*). In the case of nanorods and nanostars, quantum calculations are much more complex, but the hot-electron distributions are expected to be similar to that of a spherical nanoparticle.

In Figure S4, we show the non-equilibrium population of plasmonic electrons, $\delta n(E) = n(E) - n_{0,F}(E)$, where $n_{0,F}(E)$ is the Fermi distribution of electrons over energy. The function $\delta n(E)$ is positive above the Fermi level and negative below the Fermi level. These positive and negative intervals describe the generation of hot electrons and hot holes, respectively. Hot holes are generated below the Fermi sea and represent empty (unpopulated) quantum states. Important features, which we can see in the hot-electron region above the Fermi sea in Figure S4, are an intensive peak near the Fermi level and a plateau in the interval of energies $E_F < E < E_{\max} = E_F + \hbar\omega$, where E_F and $\hbar\omega$ are the Fermi energy and the photon energy quantum, respectively. The intensive peak describes the Drude electrons that form the standing plasmonic wave; these electrons can be described by the classical theory based on the dynamic Drude conductivity. The plateau describes the hot electrons with high energies in the standing plasmonic wave. The generation of such hot electrons is a quantum effect appearing near the surface of the plasmonic nanocrystal. The physical origin of generation of hot electrons is in the non-conservation of linear momentum of electrons near the surface.

Section 5: Modeling Carrier Distribution in TiO_2

The hot carrier distribution injected in to the TiO_2 was modelled as follows. First, for the nonthermal case, the distribution calculated in Section 4 was taken as the nonthermal carrier distribution created in the TiO_2. This represents the extreme case where the injected hot carrier distribution maintains the same energetic shape as in the metal, implying an injection rate which can sustain a steady state hot carrier population. Second, for the thermal case where carriers are considered relaxed in the TiO_2, the carrier distribution was modeled by using an elevated temperature Fermi-Dirac distribution to match the thermal part of the hot carrier distribution predicted in Section 4. These two cases were included in the excited state x-ray calculation as described in Section 6, maintaining the same peak amplitude for comparison. As discussed more in the next section and the main text, the relative insensitivity of the loss function to fine structure prevents a determination of the exact nonthermal degree of the excited carrier distribution.

Section 6: Including state-filling effects in x-ray absorption

The x-ray absorption $\alpha(\omega)$ is the convolution of the joint-density of states $DOS(\omega)$ between the core level and the core-hole modified unoccupied valence states, as well as a Lorentzian $L(\omega, \Gamma(\omega))$ representing the finite lifetime $\Gamma(\omega)$ of the transition.[12] The lifetime $\Gamma(\omega)$ depends on energy and is given by an integral over the material's electron loss function, $Im[-1/\epsilon(\omega, k)]$ where k is momentum and ω the frequency of the photoexcited electron. This integral is most commonly expressed in terms of the inelastic mean free path (IMFP), λ, of the electron as[13,14]

$$\lambda^{-1}(E) = \frac{1}{\pi E}\int d\omega' \int dk \frac{1}{k} Im\left[-\frac{1}{\epsilon(\omega',k)}\right], \qquad (1)$$

where the bounds on the frequency integral go from 0 to $E - E_f$ and the bounds on the momentum integral go from $k_{\pm} = \sqrt{\frac{2mE}{\hbar^2}} \pm \sqrt{\frac{2m}{\hbar^2}(E - \hbar\omega')}$. These bounds simply describe the energy and momentum space possible to scatter into for a photoexcited electron. The energy dependent IMFP can then be converted into the energy dependent lifetime $\Gamma(E)$ including the core-hole lifetime Γ_{CH}

$$\Gamma(E) = \frac{\hbar}{\lambda(E)}\sqrt{\frac{2E}{m_e}} + \Gamma_{CH} \,. \qquad (2)$$

The x-ray absorption is then given by the convolution

$$\alpha(\omega) \sim \int d\omega' \, L\big(\omega', \Gamma(\omega')\big) * DOS(\omega), \qquad (3)$$

where the joint density of states (DOS) is calculated using OCEAN and each transition energy has an independent broadening. To include the change in the excited state occupation, the integral over energy and momentum in Equation 1 is modified to include state blocking through an energy dependent, fractional occupation that is given by the injected electron distribution. The same excited state fractional occupation is then also included in the DOS in Equation 3.

The loss function is modeled following the Penn algorithm of Reference (*13,14*), but with a momentum independent critical point contribution added near the valence band energy to account for interband transitions in the 1-10 eV range (Figure S3). A qualitative discussion of the absolute carrier injection is nullified by the relative-independence of the loss-function and the multiple convolutions. For the larger percent change in the nanorod, further corrections to the x-ray absorption description may be needed. It was assumed here that the loss function was only changed by the blocking of momentum and energy scattering at the excited carrier energies. The charge equilibration and interaction of hot-holes makes it possible the plasmon poles in the loss function were modified as the valence charge density changed.

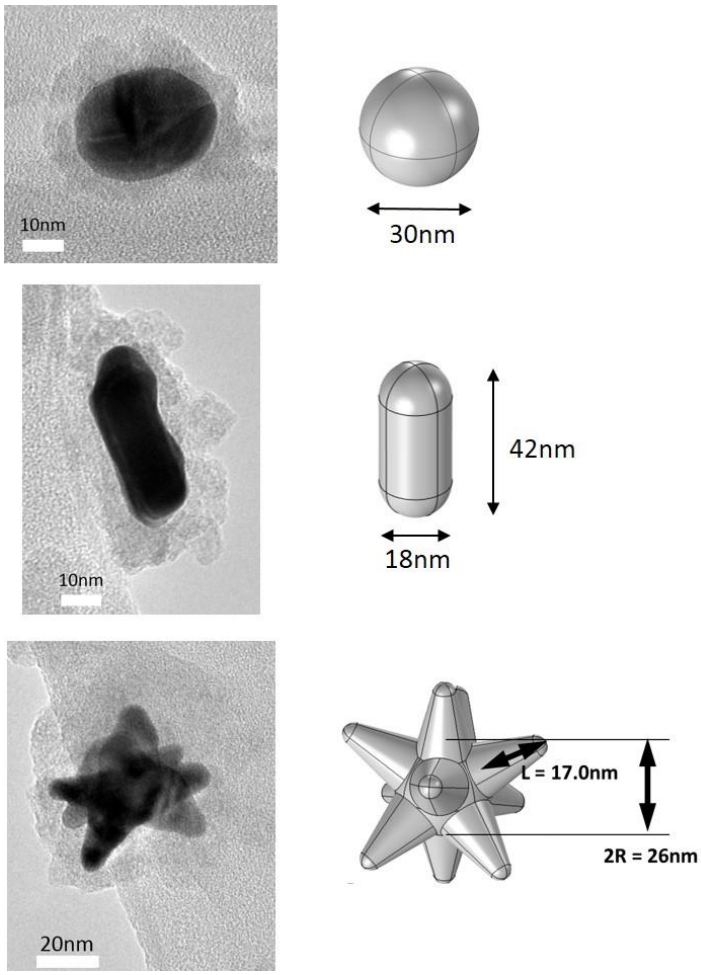

Figure S1. Characterization of Plasmonic Core Shell Nanoparticles and Theoretical Model. The left side panels show the metal nanoparticle core as the darker shaded region, while the TiO_2 shell is the more transparent region. The right side panels show the theoretical models used to mimic the experimentally measured core-shell nanoparticles.

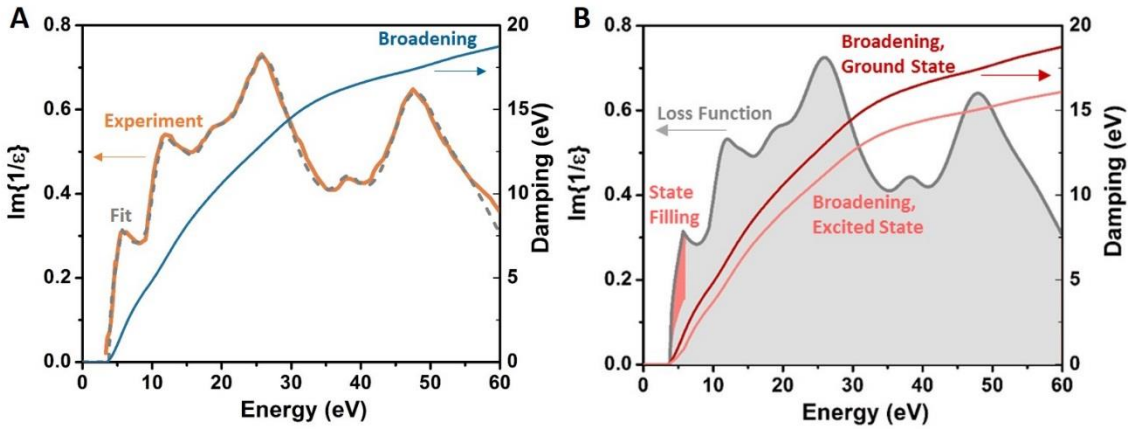

Figure S2. Broadening of X-ray Absorption (**A**) Loss function, model, and resulting energy dependent lifetime for TiO_2. The resulting broadening is determined by the photoexcited electron's inelastic mean free path, calculated from the loss function by integrating over the available energy and momentum scattering space. (**B**) After excitation, state-filling blocks the available scattering pathways, changing the linewidth of the transition. The blocking of transitions after excitation are shown in the light shade of red for the loss function, with the resulting change in broadening shown as the light red line.

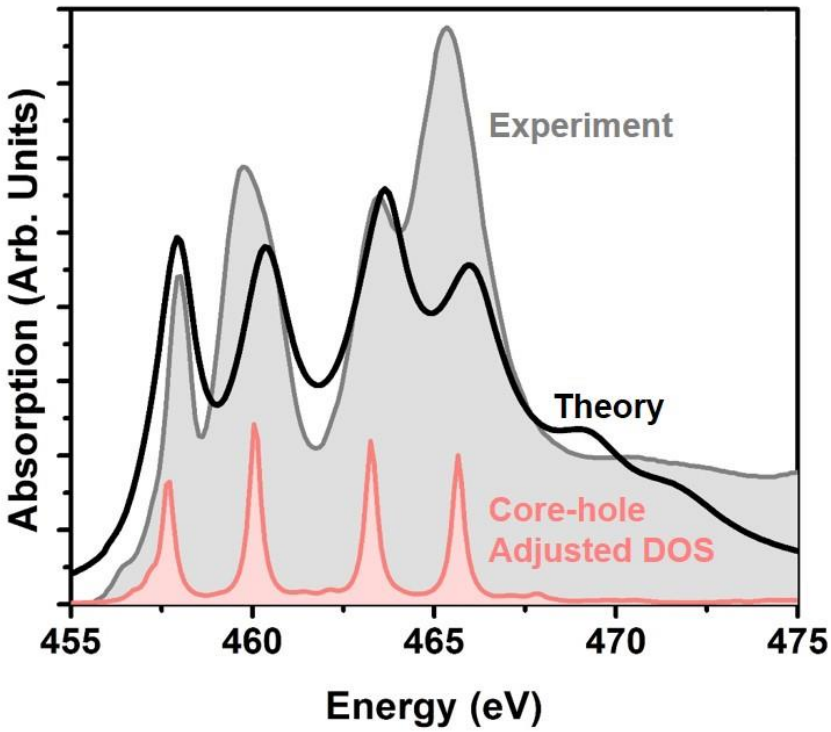

Fig. S3. Experimental and Predicted Ground State Absorption for TiO_2. The calculations are detailed in Section 3 and 6. In brief, the core-hole adjusted density of states (DOS) are calculated using the OCEAN code. This code uses the Bethe-Salpeter equation to predict the multiplet splitting effects caused by the core-hole. Broadening of the DOS is then included using the loss function as described in Figure S2 and Section 6.

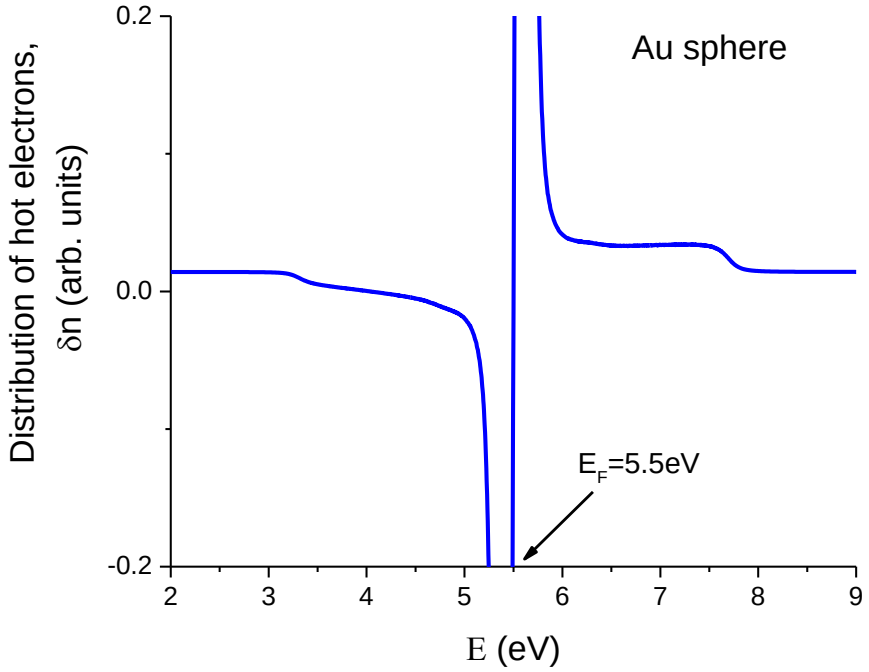

Fig. S4. Theoretically Predicted Generic Hot Electron (Positive) And Hole (Negative) Population in the Metal. This distribution was calculated for the photon energy 2.2eV for a spherical Au nanoparticle.

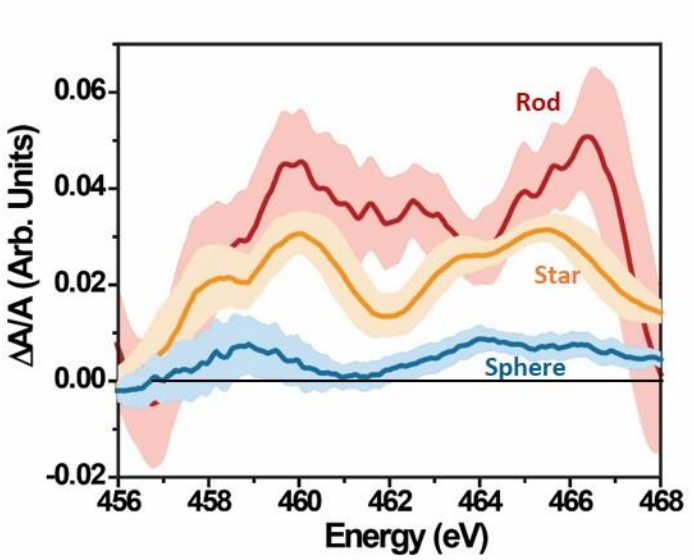

Fig. S5. Change in Experimental Absorption without Continuum Background Removed.

References

1. Cushing, S. K.; Li, J.; Bright, J.; Yost, B. T.; Zheng, P.; Bristow, A. D.; Wu, N. Controlling Plasmon-Induced Resonance Energy Transfer and Hot Electron Injection Processes in Metal@TiO_2 Core–Shell Nanoparticles. *J. Phys. Chem. C* **2015,** *119***,** 16239-16244.
2. Vinson, J.; Rehr, J. J.; Kas, J. J.; Shirley, E. L. Bethe-Salpeter Equation Calculations of Core Excitation Spectra. *Phys. Rev. B* **2011**, *83*, 115106.
3. Gilmore, K.; Vinson, J.; Shirley, E. L.; Prendergast, D.; Pemmaraju, C. D.; Kas, J. J.; Vila, F. D.; Rehr, J. J. Efficient Implementation of Core-Excitation Bethe–Salpeter Equation Calculations. *Comput. Phys. Commun.* **2015**, *197*, 109.
4. Giannozzi, P.; Baroni, S.; Bonini, N.; Calandra, M.; Car, R.; Cavazzoni, C.; Ceresoli, D.; Chiarotti, G. L.; Cococcioni, M.; Dabo, I.; Dal Corso, A.; de Gironcoli, S.; Fabris, S.; Fratesi, G.; Gebauer, R.; Gerstmann, U.; Gougoussis, C.; Kokalj, A.; Lazzeri, M.; Martin-Samos, L. et al. Quantum Espresso: A Modular and Open-Source Software Project for Quantum Simulations of Materials. *J. Phys.: Condens. Matter*. **2009**, *21*, 395502.
5. Shirley, E. L. Local Screening of a Core Hole: A Real-Space Approach Applied to Hafnium Oxide. *Ultramicroscopy* **2006**, *106*, 986.
6. Levine, Z. H.; Louie, S. G. New Model Dielectric Function and Exchange-Correlation Potential for Semiconductors and Insulators. *Phys. Rev. B* **1982**, *25*, 6310.
7. Johnson, P. B; Christy, R. W. Optical Constants of the Noble Metals. *Phys. Rev. B* **1972**, *6*, 4370−4379.

8. Kuzyk, A.; Schreiber, R.; Zhang, H.; Govorov, A.O.; Liedl, T.; Liu, N. Reconfigurable 3D Plasmonic Metamolecules. *Nat. Mater.* **2014**, *13*, 1–5.

9. Govorov, A. O.; Zhang, H.; Demir, H. V.; Gun'ko, Y. K. Photogeneration of Hot Plasmonic Electrons with Metal Nanocrystals: Quantum Description and Potential Applications. *Nano Today* **2014**, *9*, 85−101.

10. Kong, X. T.; Wang, Z.; Govorov, A.O. Plasmonic Nanostars with Hot Spots for Efficient Generation of Hot Electrons Under Solar Illumination. *Adv. Opt. Mater.* **2017**, *5*, 1600594.

11. Besteiro, L. V.; Govorov, A. O. Amplified Generation of Hot Electrons and Quantum Surface Effects in Nanoparticle Dimers with Plasmonic Hot Spots. *J. Phys. Chem. C* **2016,** *120*, 19329–19339.

12. De Groot, F.; Kotani, A. *Core Level Spectroscopy of Solids*; CRC Press: Florida, 2008, pp 93-144.

13. Penn, D. R. Electron Mean-Free-Path Calculations Using a Model Dielectric Function. *Phys. Rev. B* **1987,** *35*, 482.

14. Fuentes, G. G.; Elizalde, E.; Yubero, F.; Sanz, J. M. Electron Inelastic Mean Free Path for Ti, TiC, TiN and TiO_2 as Determined by Quantitative Reflection Electron Energy-Loss Spectroscopy. *Surf. Interface Anal.* **2002**, *33*, 230-237.